Constraints on the two-dimensional pseudospin-$\frac{1}{2}$ Mott insulator description of Sr$_2$IrO$_4$

B. Zwartsenberg[1,2] R. P. Day,[1,2] E. Razzoli,[1,2] M. Michiardi,[1,2,3] M. X. Na,[1,2] G. Zhang[4] J. D. Denlinger,[5] I. Vobornik,[6] C. Bigi,[7] B. J. Kim,[8,9,10] I. S. Elfimov,[1,2] E. Pavarini,[11,12,*] and A. Damascelli[1,2,†]

[1]*Quantum Matter Institute, University of British Columbia, Vancouver, Canada BC V6T 1Z4*
[2]*Department of Physics and Astronomy, University of British Columbia, Vancouver, Canada BC V6T 1Z1*
[3]*Max Planck Institute for Chemical Physics of Solids, Nöthnitzer Straße 40, 01187 Dresden, Germany*
[4]*Key Laboratory of Materials Physics, Institute of Solid State Physics, HFIPS, Chinese Academy of Sciences, Hefei 230031, People's Republic of China*
[5]*Advanced Light Source, Lawrence Berkeley National Laboratory, Berkeley, California 94720, USA*
[6]*Istituto Officina dei Materiali (IOM)-CNR, Laboratorio TASC, in Area Science Park, S.S.14, Km 163.5, I-34149 Trieste, Italy*
[7]*Dipartimento di Fisica, Universit di Milano, Via Celoria 16, I-20133 Milano, Italy*
[8]*Department of Physics, Pohang University of Science and Technology, Pohang 790-784, South Korea*
[9]*Center for Artificial Low Dimensional Electronic Systems, Institute for Basic Science (IBS), 77 Cheongam-Ro, Pohang 790-784, Republic of Korea*
[10]*Max Planck Institute for Solid State Research, Heisenbergstraße 1, D-70569 Stuttgart, Germany*
[11]*Institute for Advanced Simulation, Forschungszentrum Jülich, D-52425 Jülich, Germany*
[12]*JARA High-Performance Computing, Forschungszentrum Jülich, D-52425 Jülich, Germany*

Sr$_2$IrO$_4$ has often been described via a simple, one-band pseudospin-$\frac{1}{2}$ model subject to electron-electron interactions on a square lattice, fostering analogies with cuprate superconductors believed to be well described by a similar model. In this work we argue—based on a detailed study of the low-energy electronic structure by circularly polarized spin and angle-resolved photoemission spectroscopy combined with dynamical mean-field theory calculations—that a pseudospin-$\frac{1}{2}$ model fails to capture the full complexity of the system. We show instead that a realistic multiband Hubbard Hamiltonian, accounting for the full correlated t_{2g} manifold, provides a detailed description of the interplay between spin-orbital entanglement and electron-electron interactions and yields quantitative agreement with experiments. Our analysis establishes that the $j_{3/2}$ states make up a substantial percentage of the low-energy spectral weight, i.e., approximately 74% as determined from the integration of the j-resolved spectral function in the 0 to -1.64 eV energy range. The results in our work are of relevance not only to Ir-based materials but also more generally to multiorbital materials with closely spaced energy scales.

I. INTRODUCTION

Sr$_2$IrO$_4$ has been studied since shortly after the discovery of the cuprate superconductors [1,2], as the compound was believed to share some of its defining properties with the copper oxides. More specifically, Sr$_2$IrO$_4$ shares its structure with the superconducting "parent compound" La$_2$CuO$_4$, and it features a similar antiferromagnetic ground state [2–4]. A key difference is that the cuprates are described by a single hole in the e_g manifold, as opposed to the iridate that has a single hole in the t_{2g} manifold. In the seminal work by Kim *et al.*, it was suggested that the t_{2g} orbitals entangle into a filled $j_{\mathrm{eff}} = 3/2$, and a half filled $j_{\mathrm{eff}} = 1/2$ manifold [5]. It was quickly realized that this scenario would bring Sr$_2$IrO$_4$ even closer to the quintessential cuprate superconductor: A (pseudo-) spin-$\frac{1}{2}$ Mott insulator on a square two-dimensional lattice. Theoretical calculations predicted a superconducting state may exist in a j_{eff} pseudospin-$\frac{1}{2}$ system when electron

doped [6], with more sophisticated analyses including all t_{2g} orbitals and strong spin-orbit coupling (SOC) painting a similar picture [7,8]. Promising observations were made in experiments: It was found that the excitations of the pseudospins probed by resonant inelastic x-ray scattering (RIXS) are reminiscent of a Heisenberg model [9,10], the expected low-energy behavior for a spin-$\frac{1}{2}$ Mott insulator [11,12]. In addition, features reminiscent of doped Mott insulators, such as a v-shaped gap and a phase-separated spatial distribution, were seen in scanning tunneling microscopy (STM) [13] and a pseudogap was detected in angle-resolved photoemission spectroscopy (ARPES) [14]. Even stronger evidence was found in surface doped samples: STM and ARPES observe a gap that is reminiscent of those found in cuprate superconductors [15,16]. However, these are spectroscopic observations that are constrained to the surface, and so far no signatures of bulk superconducting behavior have been reported in the literature.

A potential factor in the explanation for the lack of superconductivity may be found in the nontrivial departure from a simple spin-$\frac{1}{2}$ scenario. We start by pointing out that the theoretical models predicting superconductivity have been
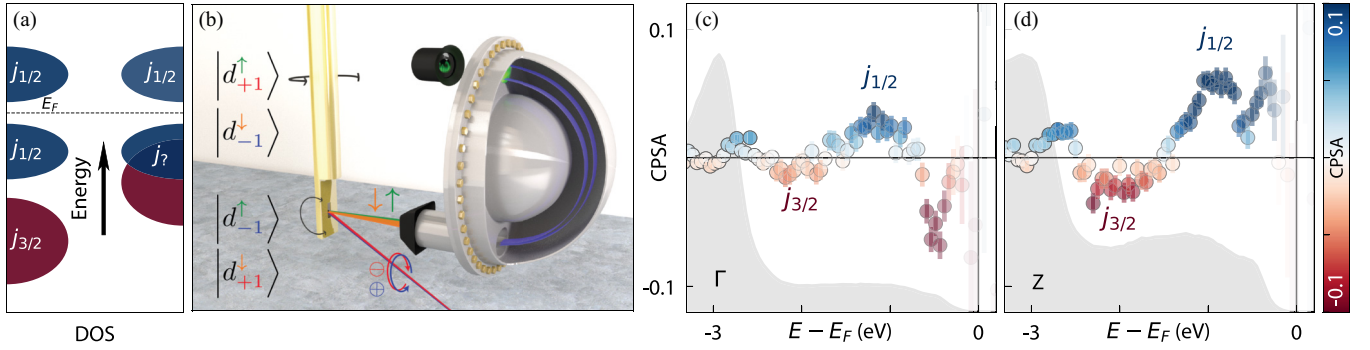
*e.pavarini@fz-juelich.de
†damascelli@physics.ubc.ca

FIG. 1. (a) Schematic representation of a fully decoupled pseudospin-$\frac{1}{2}$ model (left), and an entangled multiorbital Mott system (right). (b) Schematic depiction of the CPS ARPES experiment. Different spin-orbitally entangled states $|d_{m_\ell}^{m_s}\rangle$ can be selected by choosing a combination of circular polarization $\{\oplus, \ominus\}$ and spin-detector channel $\{\uparrow, \downarrow\}$. (c, d) The CPS ARPES intensity obtained at normal emission using 51.1 (c) and 64 (d) eV photons corresponding to the Γ and Z points in the BZ, respectively (colored markers), and the sum of spin- and polarization-dependent signals (gray shaded).

derived in the strong SOC limit [6–8] (i.e., in the limit of a "simple" pseudospin-$\frac{1}{2}$ model). Although SOC is large in this system (~ 0.45 eV [10,17,18]), it is still modest compared with the overall bandwidth (~ 2 eV) of the t_{2g} bands [19–21]. A complete splitting into $j_{3/2}$ and $j_{1/2}$ [22] multiplets is, therefore, likely not realized, and there has been some sporadic evidence that supports this idea. It was pointed out that toward the Brillouin zone (BZ) boundaries, the pristine t_{2g} character dominates the spin-orbital entanglement, and not much mixing occurs [22]. Neutron scattering shows that the local moments are far from the idealized $j_{1/2}$ picture, and in reality the eigenstates bear more resemblance to a d_{xy} orbital [23]. Taken altogether, these arguments suggest that a pseudospin-$\frac{1}{2}$ model may not be a sufficient description of the system and raise questions about the true nature of the Sr_2IrO_4 ground state.

In this paper, we use a technique that can directly attend to the question of whether a pseudospin-$\frac{1}{2}$ model is indeed a valid description for Sr_2IrO_4. In order to do this, we measure the spin-orbital entanglement of the valence band states, i.e., the expectation value $\langle \mathbf{L} \cdot \mathbf{S} \rangle$ for the low-energy states, using circularly polarized spin-ARPES (CPS-ARPES) and observe a clear departure from the canonical $j_{1/2}$ model. We are instead able to explain our observations using dynamical mean-field theory (DMFT) calculations, which accurately predict the nontrivial behavior of this multiband, spin-orbit coupled Mott system, without imposing a predefined hierarchy onto the magnitudes of these effects. Our conclusion is that a spin-$\frac{1}{2}$ model is insufficient to capture all intricacies of the low-energy electronic structure of this material, but more importantly that we gain a strong understanding of Sr_2IrO_4 by comparing our experiments with an adequately powerful theoretical description.

To make substantiated arguments about the sufficiency of the $j_{1/2}$ model, the quantum number j should be measured for the low-energy manifold, giving a distinct character for the $j_{1/2}$ and $j_{3/2}$ states. If the system can be described as a pseudospin-$\frac{1}{2}$ system, the $j_{3/2}$ states must be far enough into the valence bands so that they do not overlap with, or couple to, the $j_{1/2}$ states [Fig. 1(a), left]. A sizable overlap or coupling would result in bands with both $j_{1/2}$ and $j_{3/2}$ character

[Fig. 1(a), right]. However, while the quantum number j is not directly accessible in ARPES measurements, the alignment of spin and orbital angular momentum $\langle \mathbf{L} \cdot \mathbf{S} \rangle$, which has an immediate relation to j, can be measured directly. For a pure $j_{1/2}$ state this quantity should be positive ($\langle \mathbf{L} \cdot \mathbf{S} \rangle = 1$), whereas it would be negative for a pure $j_{3/2}$ state ($\langle \mathbf{L} \cdot \mathbf{S} \rangle = -\frac{1}{2}$) [24].

II. CPS-ARPES

To quantify the spin-orbital entanglement, spin-resolved measurements are performed using circularly polarized light, as schematically depicted in Fig. 1(b). This technique has been used previously in angle-integrated photoemission [25,26] as well as in ARPES on Sr_2RuO_4 [27] and iron pnictides [28]. The use of circularly polarized light selects a particular m_ℓ value $\{-1, +1\}$ through the photoemission dipole matrix element, while the spin-detector selects between states with $m_s = \{\uparrow, \downarrow\}$. By combining these two filters and measuring the four individual components, it is possible to obtain the spin-orbital entanglement. In particular, it can be shown that at normal emission, the z component of $\langle \mathbf{L} \cdot \mathbf{S} \rangle$, i.e., $\langle L_z S_z \rangle$, can be recovered.

To derive this property, we start by considering the photoemission dipole matrix element arising from Fermi's golden rule (for a thorough review, the reader is referred to Ref. [29]),

$$M_{i,f}^{\varepsilon,\sigma,k} = \langle \psi_f^k | \mathbf{r} \cdot \boldsymbol{\varepsilon} | \phi_i \rangle$$

$$= \sum_{\substack{\ell_i, \ell_f, m_i \\ m_\varepsilon, m_f}} c_{\ell_i}^{m_i} B_{n_i, \ell_i, \ell_f} \langle Y_{\ell_i}^{m_i} | Y_1^{m_\varepsilon} | Y_{\ell_f}^{m_f} \rangle Y_{\ell_f}^{m_f}(\theta_k, \phi_k), \quad (1)$$

with $|\psi_f^k\rangle$ and $|\phi_i\rangle$ as the final and initial states, respectively; $\boldsymbol{\varepsilon}$ is the polarization vector; $c_{\ell_i}^{m_i}$ is the initial state coefficient in the basis of spherical harmonics; and B_{n_i, ℓ_i, ℓ_f} is a radial integral:

$$B_{n_i, \ell_i, \ell_f} = \int dr\, r^3 R_{n_i, \ell_i}(r) j_{\ell_f}(r), \quad (2)$$

where $R_{n_i, \ell_i}(r)$ is the radial part of the basis functions and $j_{\ell_f}(r)$ are the spherical Bessel functions. Using circularly polarized light with positive helicity gives $\boldsymbol{\varepsilon}^\oplus \cdot \mathbf{r} = \varepsilon_0(\mathbf{x} + i\mathbf{y}) =$
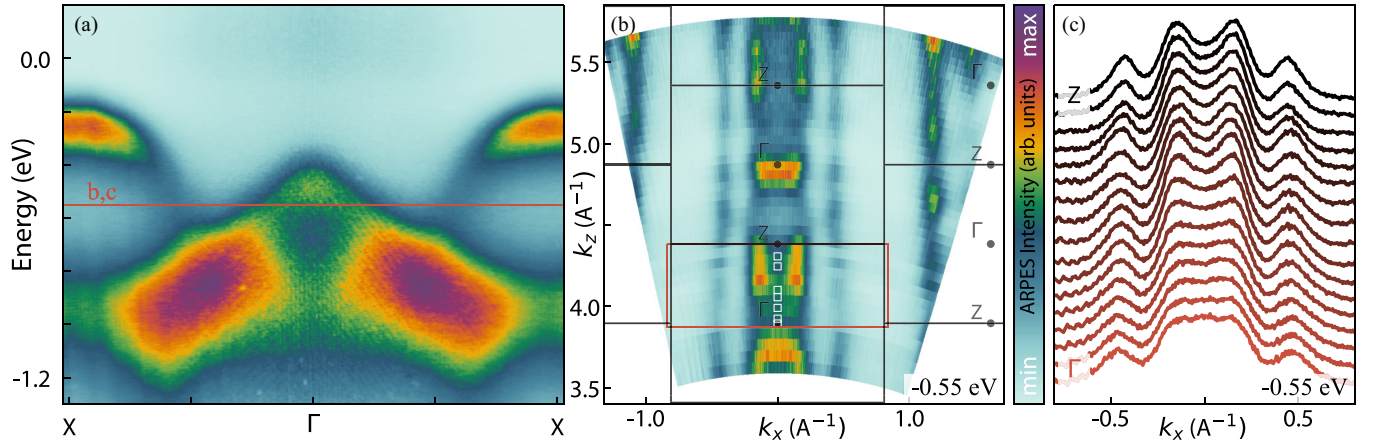
FIG. 2. Overview of photon energy-dependent results in Sr_2IrO_4. (a) Spectrum at $h\nu = 100$ eV ($k_z = 5.29$ Å^{-1}). The red line indicates the energy ($E = -0.55$ eV) at which the plots presented in panels (b) and (c) have been generated. (b) Constant energy map at $E = -0.55$ eV, using a sum of σ- and π-polarized light. The white boxes indicate the positions of later presented CPS-ARPES data. (c) A series of MDCs measured with photon energies ranging from $h\nu = 51$ eV ($k_z = 3.89$ Å^{-1}) to $h\nu = 84$ eV ($k_z = 4.87$ Å^{-1}), with σ-polarization at $E = -0.55$ eV; the (k_x, k_z) area encompassed is indicated by a red box in (b).

$\varepsilon_0 Y_1^1$. The matrix element then becomes

$$M_{i,f}^k = \langle \psi_f^k | \mathbf{r} \cdot \boldsymbol{\varepsilon} | \phi_i \rangle$$

$$= \varepsilon_0 \sum_{\substack{\ell_f \\ m_f, m_i}} c_{l_i}^{m_i} B_{n_i, \ell_i, \ell_f} \langle Y_{\ell_f}^{m_f} | Y_1^1 | Y_{\ell_i}^{m_i} \rangle Y_{l_f}^{m_f}(\theta_k, \phi_k). \quad (3)$$

At the Γ point, we can simplify this equation by using the fact that the spherical harmonic $Y_{l_f}^{m_f}(\theta_k, \phi_k)$ has nodes for all m_f except $m_f = 0$, where its value is 1. With the spherical harmonic arising from the polarization vector set to Y_1^1, we only emit from a single initial state spherical harmonic. We can, therefore, simplify the expression in Eq. (3) to

$$M_{i,f}^{k\sigma} = \varepsilon_0 \sum_{\ell_f} c_{\ell_i}^{m_i = -1, \sigma} B_{n_i, \ell_i, \ell_f} \langle Y_{\ell_f}^0 | Y_1^1 | Y_{\ell_i}^{-1} \rangle. \quad (4)$$

Noting that the product of spherical harmonics does not depend on m_i, we can take the sum over ℓ_f up into a constant prefactor. We denote $a_{\ell_i, \ell_f} = \langle Y_{\ell_f}^0 | Y_1^1 | Y_{\ell_i}^{-1} \rangle$. To get the photoemission intensity, we take the squared norm

$$I^{\oplus\sigma} = \varepsilon_0^2 \left(\sum_{\ell_f} B_{n_i, \ell_i, \ell_f} a_{\ell_i, \ell_f} \right)^2 |c_{\ell_i}^{m_i = -1, \sigma}|^2.$$

$$= A |c_{\ell_i}^{-1, \sigma}|^2. \quad (5)$$

It follows trivially that we can measure the other components using $\sigma = \uparrow, \downarrow$ and $\varepsilon = \oplus, \ominus$ to construct

$$I^{\ominus\uparrow} - I^{\oplus\uparrow} - I^{\ominus\downarrow} + I^{\oplus\downarrow}$$

$$= A(|c^{1,\uparrow}|^2 - |c^{-1,\uparrow}|^2 - |c^{1,\downarrow}|^2 + |c^{-1,\downarrow}|^2). \quad (6)$$

Noting that in the basis of $|m_l = 1, \uparrow\rangle, |-1, \uparrow\rangle, |1, \downarrow\rangle, |-1, \downarrow\rangle$, we have

$$L_z S_z = \frac{\hbar^2}{2} \begin{pmatrix} 1 & 0 & 0 & 0 \\ 0 & -1 & 0 & 0 \\ 0 & 0 & -1 & 0 \\ 0 & 0 & 0 & 1 \end{pmatrix}; \quad (7)$$

we get for $\langle L_z S_z \rangle$

$$\langle L_z S_z \rangle = \frac{\hbar^2}{2} (|c^{1,\uparrow}|^2 - |c^{-1,\uparrow}|^2 - |c^{1,\downarrow}|^2 + |c^{-1,\downarrow}|^2), \quad (8)$$

which is precisely the expression found in Eq. (6) aside from the prefactor. Note that the expression derived above is independent (up to the prefactor A) of the values for B_{n_i, ℓ_i, ℓ_f}. Since there is only a single term of m_{l_i} for each configuration, there are no interference terms and the sum in Eq. (5) can be evaluated separately. This formulation of $\langle L_z S_z \rangle$ in terms of $I^{\varepsilon, \sigma}$ is unfortunately only valid if all factors B_{n_i, ℓ_i, ℓ_f} are identical for both polarizations $\varepsilon^{\oplus}$ and $\varepsilon^{\ominus}$, which may not be the case in a system where there is circular dichroism. Moreover, if the sensitivity of the spin detectors is not equal for up and down channels, the description also breaks down. By denoting the sensitivity of the detector of each spin detector as η^σ and the factor related to the circular dichroism as α^ε, we can write the measured photoemission signal as

$$\tilde{I}^{\varepsilon\sigma} = \alpha^\varepsilon \eta^\sigma I^{\varepsilon, \sigma} = \alpha^\varepsilon \eta^\sigma A |c_{\ell_i}^{m_i, \sigma}|^2, \quad (9)$$

where $m_i = -1$ for $\varepsilon^{\oplus}$ and 1 for $\varepsilon^{\ominus}$. Substituting the $\tilde{I}$ into Eq. (6), the expectation value $\langle L_z S_z \rangle$ is no longer recovered as a result of the prefactors. We can, instead, take advantage of the geometric mean P which divides out the prefactors

$$P = \frac{\sqrt{\tilde{I}^{\ominus\uparrow}\tilde{I}^{\oplus\downarrow}} - \sqrt{\tilde{I}^{\oplus\uparrow}\tilde{I}^{\ominus\downarrow}}}{\sqrt{\tilde{I}^{\ominus\uparrow}\tilde{I}^{\oplus\downarrow}} + \sqrt{\tilde{I}^{\oplus\uparrow}\tilde{I}^{\ominus\downarrow}}}$$

$$= \frac{\sqrt{|c^{1,\uparrow}|^2|c^{-1,\downarrow}|^2} - \sqrt{|c^{-1,\uparrow}|^2|c^{1,\downarrow}|^2}}{\sqrt{|c^{1,\uparrow}|^2|c^{-1,\downarrow}|^2} + \sqrt{|c^{-1,\uparrow}|^2|c^{1,\downarrow}|^2}}. \quad (10)$$

In the case of Kramers degeneracy, we should have $|c^{m,\sigma}|^2 = |c^{-m,\bar{\sigma}}|^2$, and using the fact that the states are normalized ($\sum |c^{m,\sigma}|^2 = 1$) we obtain

$$P = \frac{|c^{1,\uparrow}|^2 - |c^{1,\downarrow}|^2}{|c^{1,\uparrow}|^2 + |c^{1,\downarrow}|^2}$$

$$= |c^{1,\uparrow}|^2 - |c^{1,\downarrow}|^2 - |c^{-1,\uparrow}|^2 + |c^{-1,\downarrow}|^2 = \frac{2}{\hbar^2} \langle L_z S_z \rangle. \quad (11)$$

Using the geometric mean, we can thus extract the expectation value for $\langle L_z S_z \rangle$ without the need to know the exact detector sensitivities or circular dichroism effects.

III. EXPERIMENTAL RESULTS

Spin-resolved measurements were performed at the VESPA endstation [30] at the Elettra Sincrotrone Trieste using VLEED spin detectors. We present the result of applying CPS-ARPES to Sr_2IrO_4 in Figs. 1(c) and 1(d), which display the observed CPS-ARPES intensity (colored markers) at normal emission using 51.1 eV (Γ) and 64 eV (Z) photons, respectively. The gray-shaded curves represent the sums of all signals (corresponding to spin-integrated ARPES). Comparing panels (b) and (c, d) we can readily identify various features: Negative (-2 eV) and positive (-1 eV) regions belonging, respectively, to states with $j_{3/2}$ and $j_{1/2}$ character. Although the data from the Z point in the BZ [Fig. 1(d)] are in line with a simple pseudospin-$\frac{1}{2}$ picture, the strong negative signal around $E = -0.5$ eV at the Γ point [Fig. 1(c)] appears to be inconsistent. In the remainder of the paper we will show that this indeed constitutes a violation of the pseudospin-$\frac{1}{2}$ picture.

First we will provide a more detailed analysis along different crystal momenta to capture a more complete picture of the spin-orbital entanglement. We note that while it is possible to measure CPS-ARPES along the in-plane momentum (k_x, k_y), data taken this way are much more challenging to interpret. We have nevertheless measured in-plane CPS-ARPES for which the data and corresponding analysis can be seen in full in the Appendix. Here instead we focus our attention on k_z, also in light of the puzzling results in Fig. 1. In ARPES measurements, the perpendicular momentum (k_z) is accessible through changing the incident photon energy. Although Sr_2IrO_4 is quasi-two-dimensional, the extended Ir $5d$ orbitals have the potential to magnify the out-of-plane hopping. The k_z dispersion in Sr_2IrO_4 and the related bilayer $Sr_2Ir_2O_7$ compound has been studied previously [31], and a modest energy dispersion was observed at the X point. However, no data have been presented at normal emission, which is where our study is concerned.

To provide some context for the forthcoming CPS-ARPES data, we first consider spin-integrated photon energy-dependent ARPES data. Photon energy-dependent spin-integrated ARPES measurements presented here were taken at the MERLIN beamline of the Advanced Light Source. Data were acquired between 50 and 120 eV. The data are corrected using an inner potential [32] $V_0 = 11$ eV, in good agreement with earlier published results [31]. We plot a valence band mapping of Sr_2IrO_4 along the $\Gamma - X$ in Fig. 2(a). A constant energy map at $E = -0.55$ eV in the $k_z - k_x$ plane is displayed in Fig. 2(b) for a sum of π and σ polarization. The modulated intensity changes, especially those periodic in k_z, are a clear sign of interlayer coupling and of an underlying k_z dispersion. A closer inspection reveals pinching of the cylindrical state around Γ, which becomes particularly clear when considering momentum distribution curves (MDCs) between Γ and Z [Fig. 2(c)]. Although we find clear evidence of k_z dispersion in the exposition of MDCs, the broad nature of the bands makes observing a simple periodic oscillation in
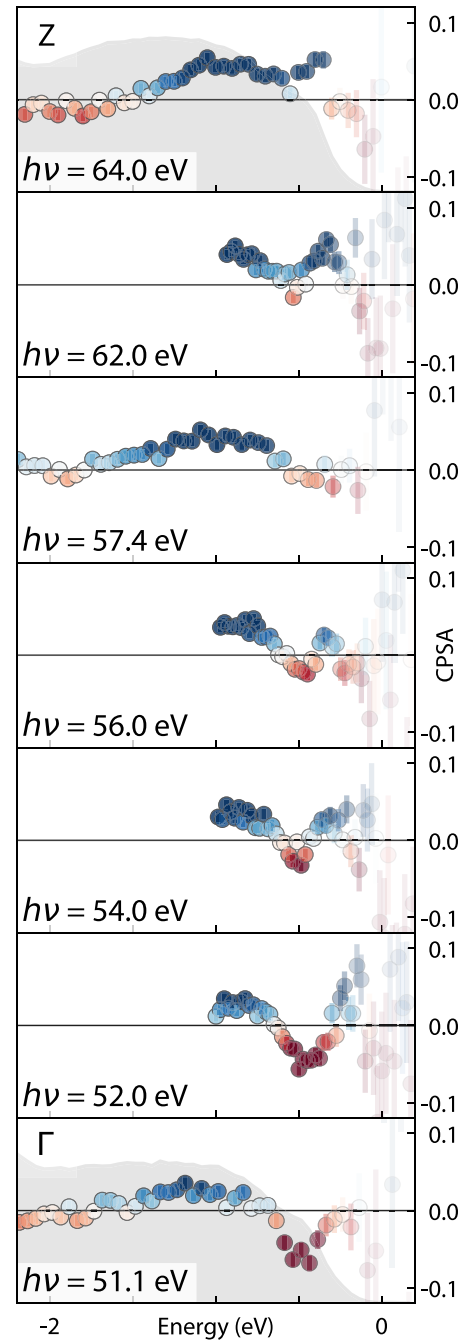

FIG. 3. CPS-ARPES measurements (colored markers) for photon energies ranging from 51.1 to 64 eV. The sum of spin- and polarization-dependent signals (gray shaded) correspond to spin-integrated ARPES.

the corresponding energy distribution curves more challenging. We also note that the energy scale appears significantly smaller than the in-plane bandwidth ($\sim$1–2 eV), or even the SOC parameter ($\sim$0.45 eV); however, as pointed out in previous work on Sr_2RuO_4 [27], states close to degeneracies can undergo significant changes as a result of SOC effects, which in turn can lead to a remarkable k_z dependence of the character of the eigenstates even though a sizable energy dispersion is notably absent.
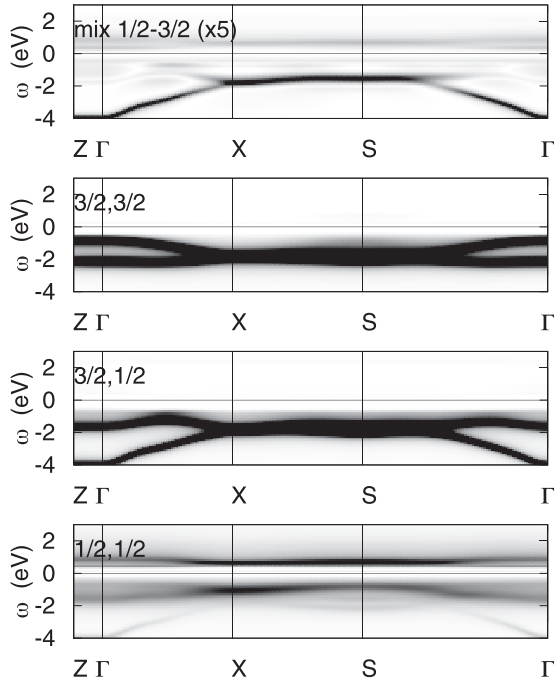
FIG. 4. Diagonal and off-diagonal components of the spectral function in the j basis.

We now return to CPS-ARPES experiments, focusing purely on normal emission measurements and changing k_z only through adjusting the photon energy of the incident beam. We would like to reiterate that in this case the CPS-ARPES measurement is directly proportional to the expectation value of $\langle L_z S_z \rangle$, and photoemission matrix element effects cancel out completely. Photon energy-dependent CPS-ARPES results are presented in Fig. 3 as colored markers. A gray background indicates the sum of all four individual spin- and light-polarization-dependent signals, which corresponds to spin-integrated photoemission. The progression of the CPS-ARPES signal is evident and provides context and additional proof for the puzzling result first presented in Fig. 1. Although the positive and negative signal around $E = -1$ and $-2\,\text{eV}$ is present in all the spectra, the data at low binding energies paint a contrasting picture. The peak in the spectrum at $E = -0.5\,\text{eV}$ that starts out negative in Fig. 3 at 51.1 eV (Γ) can be seen to change sign as the photon energy increases to 64 eV (Z). It should be stressed that this is an important result: The character of the spin-orbital entanglement of the lowest-energy band changes from parallel to antiparallel upon varying k_z, revealing a drastic change in the character of the lowest-energy eigenstates. Neither this sign reversal nor the negative signal observed at Γ is reconcilable with a simple pseudo-spin model and it requires us to rethink our description of the low-energy states of Sr_2IrO_4.

IV. COMPARISON TO DMFT

We now attempt to shed light on our observations by constructing and solving a model that goes beyond the pseudospin-$\frac{1}{2}$ framework. To this end, we turn to DMFT calculations for a realistic multiband Hubbard Hamiltonian. The

method adopted can be summarized as follows. We calculate the electronic structure (including spin-orbit effects) in the local-density approximation (LDA) via the full-potential linearized augmented plane-wave method, as implemented in the WIEN2k code [33]. A set of t_{2g} Wannier functions centered at the Ir atoms and spanning the t_{2g} bands is then constructed. In this basis we build the system-specific t_{2g} Hubbard model:

$$\hat{H} = -\sum_{ii'} \sum_{mm'} \sum_{\sigma\sigma'} t^{i,i'}_{m\sigma,m'\sigma'} \hat{c}^\dagger_{im\sigma} \hat{c}_{i'm'\sigma'}$$

$$+ \frac{1}{2} \sum_{i} \sum_{mm'pp'} \sum_{\sigma\sigma'} U_{mm'pp'} \hat{c}^\dagger_{im\sigma} \hat{c}^\dagger_{im'\sigma'} \hat{c}_{ip'\sigma'} \hat{c}_{ip\sigma}. \quad (12)$$

In the Hamiltonian above, $\hat{c}^\dagger_{im\sigma}$ ($\hat{c}_{im\sigma}$) creates (annihilates) an electron at lattice site i with spin $\sigma \in \{\uparrow, \downarrow\}$ and orbital $m \in \{xy, yz, xz\}$. The parameters $-t^{i,i}_{m\sigma,m'\sigma'}$ define the on-site crystal-field matrix, including local spin-orbit terms; the intersite ($i \neq i'$) terms $-t^{i,i'}_{m\sigma,m'\sigma'}$ are the hopping integrals, also with spin-orbit interaction contributions. The key screened Coulomb integrals are the direct Coulomb interaction, $U_{mm'mm'} = U_{m,m'} = U - 2J(1 - \delta_{m,m'})$, the exchange Coulomb interaction $U_{mm'm'm} = J$, the pair-hopping term, $U_{mmm'm'} = J$, and the spin-flip term $U_{mm'm'm} = J$. We adopt the values $(U, J) = (3.2, 0.4)\,\text{eV}$, corresponding to an average Coulomb repulsion of $U_{\text{avg}} = 2.4\,\text{eV}$; this reproduces the small insulating gap well, as we have shown in Ref. [34]. We solve (12) with DMFT using the interaction-expansion continuous time quantum Monte Carlo impurity solver, in the implementation developed in Refs. [35–37]. The calculations presented have been performed at the electronic temperature 290 K. We obtain the orbital and **k**-resolved spectral-function matrix using the maximum-entropy method. In Fig. 4 we show

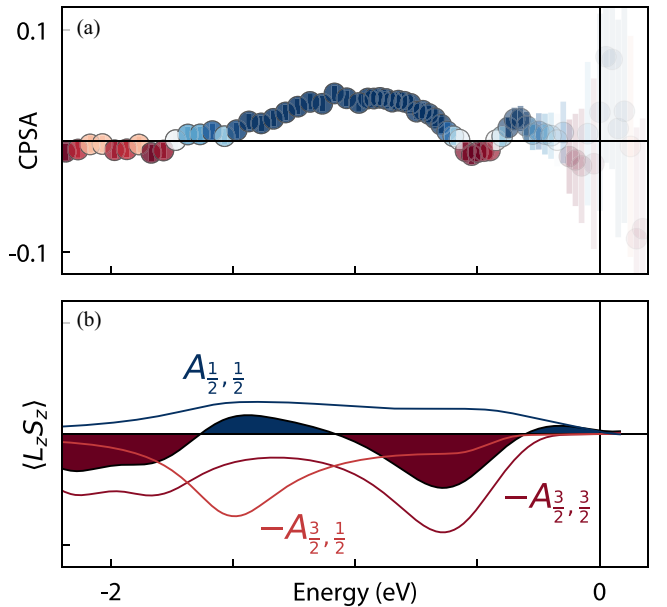FIG. 5. Comparison between experiment and DMFT. (a) k_z integrated CPS-ARPES data at normal emission. (b) LDA + DMFT calculations for Sr_2IrO_4 with Coulomb parameters $U = 3.2\,\text{eV}$ and $J = 0.4\,\text{eV}$. Bare lines correspond to diagonal elements $A_{j,m_j}(\mathbf{k};\omega)$ of the spin-orbital resolved spectral function in the j basis at the Γ point. The filled colored curve shows the calculated $\langle L_z S_z \rangle$.
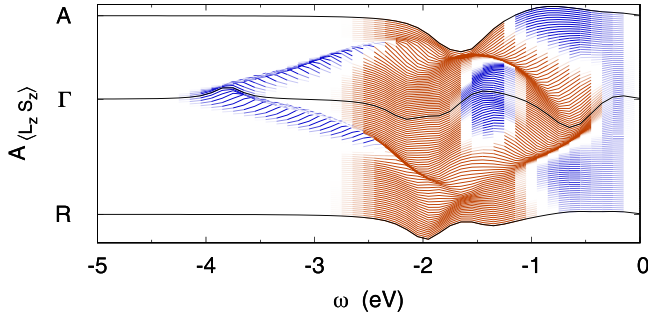
FIG. 6. Evolution of $\langle L_z S_z \rangle$ along the directions $\Gamma - A$ and $\Gamma - R$, where $A = (\pi/a, \pi/a, \pi/c)$ and $R = (0, \pi/a, \pi/c)$.

the weight of each component along high-symmetry lines of the BZ. The k_z dispersion itself is small and difficult to resolve, but the shift in character with energy is very clear at any k point. From here we calculate

$$\mathcal{A}_{\langle L_z S_z \rangle} = \tfrac{1}{4}(A_{1,1}^{\uparrow} + A_{-1,-1}^{\downarrow} - A_{1,1}^{\downarrow} - A_{-1,-1}^{\uparrow}), \quad (13)$$

where $A_{m,m}^{\sigma}$ is the spectral function for orbital m and spin σ. In the basis of the $j = 1/2$ and $j = 3/2$ states

$$\mathcal{A}_{\langle L_z S_z \rangle} = -\frac{1}{2}A_{\frac{3}{2};\frac{3}{2}} + \frac{1}{6}A_{\frac{3}{2};\frac{1}{2}} + \frac{1}{3}A_{\frac{1}{2};\frac{1}{2}} + \frac{\sqrt{2}}{3}B_{\frac{3}{2},\frac{1}{2};\frac{1}{2}}, \quad (14)$$

where $A_{j;m_j}$ are the diagonal elements of the spectral-function matrix in the j basis, while $B_{j,j';m_j}$ is an off-diagonal element ($j = j' \pm 1/2$, $m_j = m_{j'} = 1/2$); the latter turns out to be small at low energy.

This provides a full description of the t_{2g} manifold, which can recover a pseudospin-$\frac{1}{2}$ system as a special case but covers a broader class of potential models. Such models combined with photoemission have previously been used to gain significant understanding of Sr_2RuO_4, which shares a similar amount of complexity associated with its low-energy structure [36,38]. The measured CPS-ARPES intensity is proportional to $\mathcal{A}_{\langle L_z S_z \rangle}$. Along ΓZ, only $A_{\frac{3}{2};\frac{3}{2}}$ and $A_{\frac{1}{2};\frac{1}{2}}$ contribute sizably at very low energy and thus determine the sign of $\mathcal{A}_{\langle L_z S_z \rangle}$. Since the small k_z dispersion is hard to resolve in our DMFT calculations, for a quantitative analysis in Fig. 5 we compare the DMFT results with CPS-ARPES spectra integrated over the k_z axis, finding excellent agreement. Barring the precise energies where the sign of $\langle L_z S_z \rangle$ changes, all the positive and negative regions—including the unexpected negative peak around $E = -0.5$ eV—are reproduced (and in fact the quantitative agreement for the oscillating character of $\langle L_z S_z \rangle$ can be observed not only for the lowest energy states but on the full 4 eV energy window probed in the experiment). All the oscillations are present in both panels, which implies that DMFT gives an accurate representation of the band structure of Sr_2IrO_4.

It is worth pointing out that, although the exact energy where the sign changes deviates, the presence of these oscillations itself is independent of the precise values of the Coulomb parameters U and J or often adopted approximations of the Coulomb vertex, provided that they yield an insulating state. This further supports our conclusion that taking into account the multiband nature of the system is the critical starting point. Our DMFT calculations give us direct access to the projections onto the $j_{1/2}$ and $j_{3/2}$ states (shown as bare lines

in Fig. 5), allowing us to make more substantiated comments about our earlier claims: The spectral weight in the low-energy states arises approximately for 74% from $j_{3/2}$ states determined as the ratio of spectral weights integrated from the sign change in $\langle L_z S_z \rangle$ at $E = -1.64$ eV all the way up to $E = 0$ eV.

The results obtained along ΓA and ΓR are shown in Fig. 6, away from the ΓZ direction. Since these results are presented away from "normal emission," to compare these directly to experiments (i.e., Fig. 7) a more advanced treatment of the photoemission dipole matrix elements is required. From these plots, we can see that toward the zone boundaries, the overall magnitude of $\langle L_z S_z \rangle$ decreases, as we observe in Fig. 7, and has also been suggested in Ref. [21] on the basis of density-functional theory calculations.

V. CONCLUSIONS

With our experiments and accompanying DMFT analysis we have thus demonstrated that a pseudospin-$\frac{1}{2}$ model is insufficient to give a satisfying description of the system at hand. Rather, one needs to rely on a modeling in terms of at least the full t_{2g} states and electron-electron interactions. While a description in terms of $j_{1/2}$ orbitals was instrumental in developing our initial understanding of Sr_2IrO_4 and why spin-orbit coupling gives rise to an insulating ground state [5,39], it is clear that this model lacks the descriptive power needed to make further reaching conclusions; especially, connections made to the superconducting cuprates should be reevaluated in this light. Finally, and most importantly, we have demonstrated that with a carefully crafted combination of a sufficiently complete many-body computational framework and state-of-the-art experimental approaches, we can make tangible progress in understanding materials with closely intertwined energy scales such as Sr_2IrO_4.

APPENDIX A: EFFECTIVE J STATES

The j_{eff} states arise from the similarities the t_{2g} orbitals share with the p orbitals, in particular with relation to SOC.

We will construct the Hamiltonian for which we first define the t_{2g} basis

$$b_{t_{2g}} = \{d_{xy,\uparrow}, d_{xz,\uparrow}, d_{yz,\uparrow}, d_{xy,\downarrow}, d_{xz,\downarrow}, d_{yz,\downarrow}\}, \tag{A1}$$

we get for the H_{SOC}

$$H_{SOC,t_{2g}} = \frac{\lambda}{2}\begin{pmatrix} 0 & 0 & 0 & 0 & -i & 1 \\ 0 & 0 & -i & i & 0 & 0 \\ 0 & i & 0 & -1 & 0 & 0 \\ 0 & -i & -1 & 0 & 0 & 0 \\ i & 0 & 0 & 0 & 0 & i \\ 1 & 0 & 0 & 0 & -i & 0 \end{pmatrix}. \tag{A2}$$

We then consider a transformation to a new basis of "effective" $m_l \in \{-1, 0, 1\}$ (reminiscent of p) orbitals, which we define as

$$|1_{eff}\rangle = \frac{1}{\sqrt{2}}(|d_{yz}\rangle + i|d_{xz}\rangle) = i|Y_2^{-1}\rangle, \tag{A3}$$

$$|0_{eff}\rangle = -|d_{xy}\rangle = -\frac{i}{\sqrt{2}}(|Y_2^{-2}\rangle - |Y_2^2\rangle), \tag{A4}$$

$$|-1_{eff}\rangle = \frac{1}{\sqrt{2}}(-|d_{yz}\rangle + i|d_{xz}\rangle) = -i|Y_2^1\rangle. \tag{A5}$$

Within this basis, the L^+ and L_z operators become

$$L_{l_{eff}}^+ = B_{l_{eff}}^{-1} L^+ B_{l_{eff}} = \sqrt{2}\begin{pmatrix} 0 & -1 & 0 \\ 0 & 0 & -1 \\ 0 & 0 & 0 \end{pmatrix}, \tag{A6}$$

$$L_{z,l_{eff}} = B_{l_{eff}}^{-1} L_z B_{l_{eff}} = \begin{pmatrix} -1 & 0 & 0 \\ 0 & 0 & 0 \\ 0 & 0 & 1 \end{pmatrix}. \tag{A7}$$

These are identical to the respective matrices for the $\ell = 1$ orbitals, except they are multiplied by -1 and thus behave effectively as $\ell = -1$ states. If we use these $\ell = -1$ states to construct spin-orbit entangled states known as the j_{eff} states, as was first proposed in Ref. [5], we obtain as the SOC Hamiltonian

$$H_{SOC,j_{eff}} = \begin{pmatrix} 1 & 0 & 0 & 0 & 0 & 0 \\ 0 & 1 & 0 & 0 & 0 & 0 \\ 0 & 0 & -\frac{1}{2} & 0 & 0 & 0 \\ 0 & 0 & 0 & -\frac{1}{2} & 0 & 0 \\ 0 & 0 & 0 & 0 & -\frac{1}{2} & 0 \\ 0 & 0 & 0 & 0 & 0 & -\frac{1}{2} \end{pmatrix}. \tag{A8}$$

This is again equal to the SOC Hamiltonian for $\ell = 1$ states up to a minus sign. To this end, the expectation values $\langle \mathbf{L} \cdot \mathbf{S} \rangle$ are negative to what is expected from "regular" j states.

APPENDIX B: FURTHER CPS BACKGROUND

1. Data taken away from normal emission

So far, the only expectation value discussed is the one along the z direction, and the calculated expectation values are only valid at the Γ point. Despite this, the technique has been successfully applied away from Γ [28]. The equations hold true as long as not too much weight comes from final states with $m_l \neq 0$. Following the k-dependent spherical harmonic in Eq. (1), these other components have a dependence $\propto (1 - \cos^2 \theta_k)$, where θ_k is the angle of the photoemitted electron and the
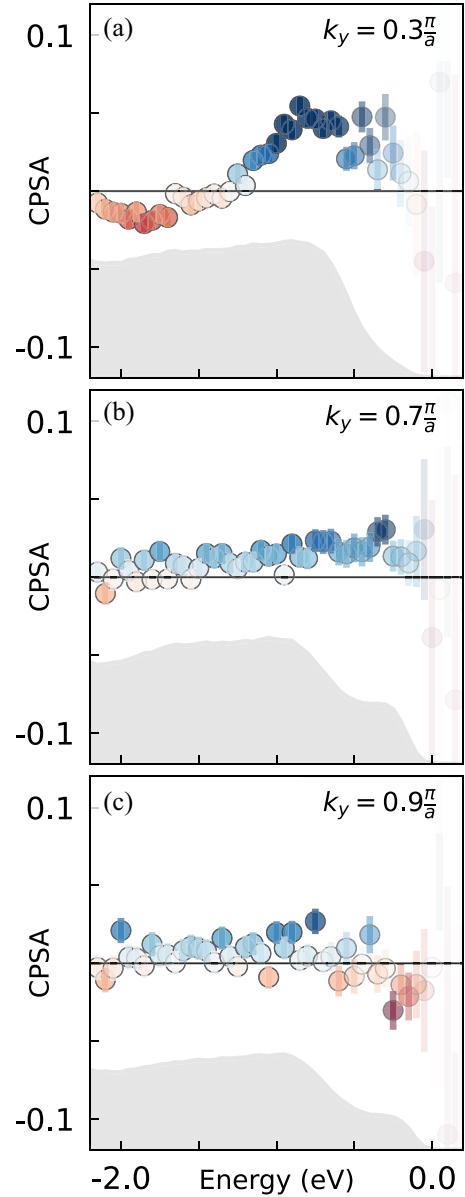

FIG. 7. [(a)–(c)] Measurement of the CPS-ARPES signal through the BZ (colored markers) and spin-integrated signal (gray line).

surface is normal. In particular, if the photon energy is large, this angle is relatively small.

2. Polarization of the incoming light

The calculations presented up to this point have assumed that the incident light is perfectly perpendicular to the surface. In the geometry of a realistic ARPES experiment, the electron analyzer would be in the light path. Therefore the incidence angle of the light is usually approximately $45°$. We will investigate here what effect such an incidence angle has on the final spectrum.

Taking the direction of the sample surface normal to be $\hat{\mathbf{z}}$, we can write for the incoming light

$$\boldsymbol{\varepsilon}^\oplus = \varepsilon_0\left(\frac{1}{\sqrt{4}}(\hat{\mathbf{x}} - \hat{\mathbf{z}}) + i\hat{\mathbf{y}}\right). \tag{B1}$$

This can be converted into spherical harmonics for which we can easily read off the equivalent normal incidence light parameters

$$\boldsymbol{\varepsilon}^{\oplus} = \frac{1}{\sqrt{4}} Y_1^0 + \left(\frac{1}{\sqrt{4}} + \frac{1}{\sqrt{8}} \right) Y_1^1 + \left(\frac{1}{\sqrt{4}} - \frac{1}{\sqrt{8}} \right) Y_1^{-1}.$$

$$(B2)$$

This deviates from the ideal case where we only make excitations with Y_1^1. However, at Γ, there are no available final state channels for Y_1^0 to scatter into. At finite emission angles θ this will generate a small unpolarized contribution that grows as $1 - \cos^2\theta$. The Y_1^{-1} term, meanwhile, creates excitations of the opposite spin-orbital entanglement. Taking the squares of these coefficients, we get 0.73, and for 0.02 for Y_1^1 and Y_1^{-1}, respectively. This means that this configuration leads to an opposite signal of just 3% at normal emission, generating a net 6% of an additional, unpolarized signal. This is far less than the approximate Sherman function [30], which is around 50% for the (high-efficiency) VLEED detectors we have used for our measurements. We can, therefore, safely ignore the angle of the incoming light.

APPENDIX C: ADDITIONAL CPS DATA

1. In-plane *k*-dependent CPS-ARPES data

To identify how the spin-orbital entanglement changes throughout the Brillouin zone, we present CPS-ARPES measurements at various points along the $(0, 0) - (0, \pi)$ direction in Fig. 7. Going away from the Γ point, the CPS-ARPES signal rapidly diminishes until the signal completely vanishes at the zone boundary. Similar observations are made if the measurements are taken along the $(0, 0) - (\pi, 0)$ direction (not shown), confirming the reliability of the measurement in this C_4 symmetric system. Previous work has suggested that the coupling into j_{eff} states is strongest at Γ, while hopping terms have a larger influence at the zone boundaries [21], which is consistent with our observations. These data support the interpretation that the spin-orbital entanglement varies through *k*-space, and in fact reduces toward the zone boundary.

2. Individual components of the CPS-ARPES signal

In order to better understand what regions in energy the features in the CPS ARPES spectra arise, it is insightful to plot the parallel ($\{|d_{+1}^{\uparrow}\rangle, |d_{-1}^{\downarrow}\rangle\}$) and antiparallel ($\{|d_{-1}^{\uparrow}\rangle, |d_{+1}^{\downarrow}\rangle\}$)
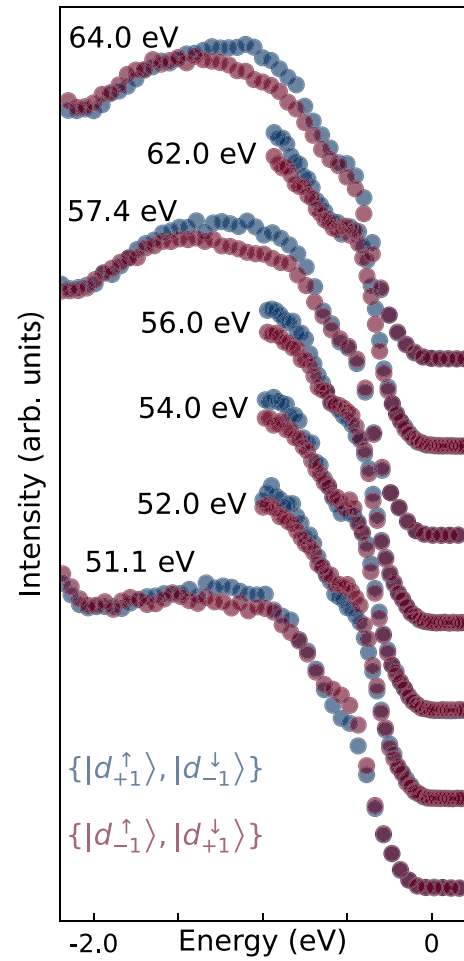

FIG. 8. Photon energy-dependent CPS-ARPES measurements, plots of the parallel (blue) and antiparallel (red) signals.

components of the spectrum, defined as

$$I_{\{|d_{+1}^{\uparrow}\rangle, |d_{-1}^{\downarrow}\rangle\}} = \sqrt{I_{\uparrow}^{\ominus} I_{\downarrow}^{\oplus}} \qquad (C1)$$

$$I_{\{|d_{-1}^{\uparrow}\rangle, |d_{+1}^{\downarrow}\rangle\}} = \sqrt{I_{\downarrow}^{\ominus} I_{\uparrow}^{\oplus}}, \qquad (C2)$$

which together form the CPS-ARPES signal as defined in the main text. These signals are plotted in Fig. 8 in blue ($I_{\{|d_{+1}^{\uparrow}\rangle, |d_{-1}^{\downarrow}\rangle\}}$) and red ($I_{\{|d_{-1}^{\uparrow}\rangle, |d_{+1}^{\downarrow}\rangle\}}$) for the same photon energies as presented in Fig. 3. From these spectra it is straightforward to see that the sign-changing signal in k_z arises from the state that appears as a shoulder around $E = -0.5$ eV.

[1] J. G. Bednorz and K. A. Müller, Z. Phys. B **64**, 189 (1986).

[2] R. J. Cava, B. Batlogg, K. Kiyono, H. Takagi, J. J. Krajewski, W. F. Peck, L. W. Rupp, and C. H. Chen, Phys. Rev. B **49**, 11890 (1994).

[3] M. K. Crawford, M. A. Subramanian, R. L. Harlow, J. A. Fernandez-Baca, Z. R. Wang, and D. C. Johnston, Phys. Rev. B **49**, 9198 (1994).

[4] G. Cao, J. Bolivar, S. McCall, J. E. Crow, and R. P. Guertin, Phys. Rev. B **57**, R11039 (1998).

[5] B. J. Kim, H. Jin, S. J. Moon, J.-Y. Kim, B.-G. Park, C. S. Leem, J. Yu, T. W. Noh, C. Kim, S.-J. Oh, J.-H. Park, V. Durairaj, G. Cao, and E. Rotenberg, Phys. Rev. Lett. **101**, 076402 (2008).

[6] F. Wang and T. Senthil, Phys. Rev. Lett. **106**, 136402 (2011).

[7] H. Watanabe, T. Shirakawa, and S. Yunoki, Phys. Rev. Lett. **110**, 027002 (2013).

[8] Z. Y. Meng, Y. B. Kim, and H.-Y. Kee, Phys. Rev. Lett. **113**, 177003 (2014).

[9] B. H. Kim, G. Khaliullin, and B. I. Min, Phys. Rev. Lett. **109**, 167205 (2012).

[10] J. Kim, D. Casa, M. H. Upton, T. Gog, Y.-J. Kim, J. F. Mitchell, M. van Veenendaal, M. Daghofer, J. van den Brink, G. Khaliullin, and B. J. Kim, Phys. Rev. Lett. **108**, 177003 (2012).

[11] M. A. Kastner, R. J. Birgeneau, G. Shirane, and Y. Endoh, Rev. Mod. Phys. **70**, 897 (1998).

[12] R. J. Birgeneau, C. Stock, J. M. Tranquada, and K. Yamada, J. Phys. Soc. Jpn. **75**, 111003 (2006).

[13] I. Battisti, K. M. Bastiaans, V. Fedoseev, A. de la Torre, N. Iliopoulos, A. Tamai, E. C. Hunter, R. S. Perry, J. Zaanen, F. Baumberger, and M. P. Allan, Nat. Phys. **13**, 21 (2017).

[14] A. de la Torre, S. McKeown Walker, F. Y. Bruno, S. Riccó, Z. Wang, I. Gutierrez Lezama, G. Scheerer, G. Giriat, D. Jaccard, C. Berthod, T. K. Kim, M. Hoesch, E. C. Hunter, R. S. Perry, A. Tamai, and F. Baumberger, Phys. Rev. Lett. **115**, 176402 (2015).

[15] Y. J. Yan, M. Q. Ren, H. C. Xu, B. P. Xie, R. Tao, H. Y. Choi, N. Lee, Y. J. Choi, T. Zhang, and D. L. Feng, Phys. Rev. X **5**, 041018 (2015).

[16] Y. K. Kim, N. H. Sung, J. D. Denlinger, and B. J. Kim, Nat. Phys. **12**, 37 (2016).

[17] L. F. Mattheiss, Phys. Rev. B **13**, 2433 (1976).

[18] S. J. Moon, H. Jin, K. W. Kim, W. S. Choi, Y. S. Lee, J. Yu, G. Cao, A. Sumi, H. Funakubo, C. Bernhard, and T. W. Noh, Phys. Rev. Lett. **101**, 226402 (2008).

[19] V. Brouet, J. Mansart, L. Perfetti, C. Piovera, I. Vobornik, P. Le Fèvre, F. Bertran, S. C. Riggs, M. C. Shapiro, P. Giraldo-Gallo, and I. R. Fisher, Phys. Rev. B **92**, 081117(R) (2015).

[20] Y. Cao, Q. Wang, J. A. Waugh, T. J. Reber, H. Li, X. Zhou, S. Parham, S.-R. Park, N. C. Plumb, E. Rotenberg, A. Bostwick, J. D. Denlinger, T. Qi, M. A. Hermele, G. Cao, and D. S. Dessau, Nat. Commun. **7**, 11367 (2016).

[21] A. Louat, F. Bert, L. Serrier-Garcia, F. Bertran, P. Le Fèvre, J. Rault, and V. Brouet, Phys. Rev. B **97**, 161109(R) (2018).

[22] To reduce the notational clutter, we will henceforth refer to the $j_{\text{eff}} = \frac{1}{2}$ and $\frac{3}{2}$ states as $j_{1/2}$ and $j_{3/2}$, respectively.

[23] J. Jeong, B. Lenz, A. Gukasov, X. Fabrèges, A. Sazonov, V. Hutanu, A. Louat, D. Bounoua, C. Martins, S. Biermann, V. Brouet, Y. Sidis, and P. Bourges, Phys. Rev. Lett. **125**, 097202 (2020).

[24] Since the j_{eff} states are constructed from $\ell_{\text{eff}} = -1$, the $\frac{1}{2}$ ($\frac{3}{2}$) state has parallel (antiparallel) alignment of spin and orbital angular momentum. A more thorough review is presented in the Appendix.

[25] D. T. Pierce and F. Meier, Phys. Rev. B **13**, 5484 (1976).

[26] T. Mizokawa, L. H. Tjeng, G. A. Sawatzky, G. Ghiringhelli, O. Tjernberg, N. B. Brookes, H. Fukazawa, S. Nakatsuji, and Y. Maeno, Phys. Rev. Lett. **87**, 077202 (2001).

[27] C. N. Veenstra, Z.-H. Zhu, M. Raichle, B. M. Ludbrook, A. Nicolaou, B. Slomski, G. Landolt, S. Kittaka, Y. Maeno, J. H. Dil, I. S. Elfimov, M. W. Haverkort, and A. Damascelli, Phys. Rev. Lett. **112**, 127002 (2014).

[28] R. P. Day, G. Levy, M. Michiardi, B. Zwartsenberg, M. Zonno, F. Ji, E. Razzoli, F. Boschini, S. Chi, R. Liang, P. K. Das, I. Vobornik, J. Fujii, W. N. Hardy, D. A. Bonn, I. S. Elfimov, and A. Damascelli, Phys. Rev. Lett. **121**, 076401 (2018).

[29] R. P. Day, B. Zwartsenberg, I. S. Elfimov, and A. Damascelli, npj Quantum Mater. **4**, 54 (2019).

[30] C. Bigi, P. K. Das, D. Benedetti, F. Salvador, D. Krizmancic, R. Sergo, A. Martin, G. Panaccione, G. Rossi, J. Fujii, and I. Vobornik, J. Synchrotron Radiat. **24**, 750 (2017).

[31] Q. Wang, Y. Cao, J. A. Waugh, S. R. Park, T. F. Qi, O. B. Korneta, G. Cao, and D. S. Dessau, Phys. Rev. B **87**, 245109 (2013).

[32] A. Damascelli, Phys. Scr. **T109**, 61 (2004).

[33] P. Blaha, K. Schwarz, G. K. H. Madsen, D. Kvasnicka, J. Luitz, R. Laskowski, F. Tran, and M. Laurence D., *WIEN2k, An Augmented Plane Wave + Local Orbitals Program for Calculating Crystal Properties* (Karlheinz Schwarz, Techn. Universität Wien, Austria, 2019).

[34] G. Zhang and E. Pavarini, Phys. Rev. B **104**, 125116 (2021).

[35] E. Gorelov, M. Karolak, T. O. Wehling, F. Lechermann, A. I. Lichtenstein, and E. Pavarini, Phys. Rev. Lett. **104**, 226401 (2010).

[36] G. Zhang, E. Gorelov, E. Sarvestani, and E. Pavarini, Phys. Rev. Lett. **116**, 106402 (2016).

[37] G. Zhang and E. Pavarini, Phys. Rev. B **95**, 075145 (2017).

[38] M. Kim, J. Mravlje, M. Ferrero, O. Parcollet, and A. Georges, Phys. Rev. Lett. **120**, 126401 (2018).

[39] B. Zwartsenberg, R. P. Day, E. Razzoli, M. Michiardi, N. Xu, M. Shi, J. D. Denlinger, G. Cao, S. Calder, K. Ueda, J. Bertinshaw, H. Takagi, B. J. Kim, I. S. Elfimov, and A. Damascelli, Nat. Phys. **16**, 290 (2020).